Check for updates

Galvanic Transformation Dynamics in Heterostructured Nanoparticles

Jingshan S. Du, Kun He, Yaobin Xu, Carolin B. Wahl, David D. Xu, Vinayak P. Dravid, Chad A. Mirkin**

J. S. Du, Dr. K. He, Dr. Y. Xu, C. B. Wahl, Prof. V. P. Dravid, Prof. C. A. Mirkin

Department of Materials Science and Engineering, Northwestern University, Evanston, IL 60208, USA
E-mail: chadnano@northwestern.edu (C.A.M.), v-dravid@northwestern.edu (V.P.D.)

J. S. Du, C. B. Wahl, D. D. Xu, Prof. V. P. Dravid, Prof. C. A. Mirkin

International Institute for Nanotechnology, Northwestern University, Evanston, IL 60208, USA

Dr. K. He, Dr. Y. Xu, Prof. V. P. Dravid
NU*ANCE* Center, Northwestern University, Evanston, IL 60208, USA

D. D. Xu, Prof. C. A. Mirkin

Department of Chemistry, Northwestern University, Evanston, IL 60208, USA

Keywords: galvanic, nanoparticles, corrosion, in situ transmission electron microscopy, multimetallic

Author Manuscript

This is the author manuscript accepted for publication and has undergone full peer review but has not been through the copyediting, typesetting, pagination and proofreading process, which may lead to differences between this version and the Version of Record. Please cite this article as doi: 10.1002/adfm.202105866.

This article is protected by copyright. All rights reserved.

Author Manuscript

Abstract: Corrosion is a significant problem for the stability of structural metals and potentially for functional nanomaterials in operating environments. When two metals with different electrochemical potentials form a junction, galvanic corrosion occurs, resulting in the sacrificial dissolution of the metal with a higher oxidation potential (lower electrode potential). Here, we show that bimetallic hetero-nanostructures composed of phase-segregated metals undergo galvanic corrosion in aqueous environments. Such selective etching of the sacrificial metal in heterojunction particles leads to the formation of unusual and kinetically stabilized half-spheroid particles. By using a fluid cell and *in situ* scanning transmission electron microscopy, we could observe a two-stage corrosion process where the Cu experiences a fractal breakdown before the Ag corrodes due to the lack of a protective oxide layer. However, when treated with a mild Ar plasma, the stability of these structures against corrosion is enhanced due to the conversion of the amorphous native oxide to a denser, thin layer of CuO on the Cu surface. Taken together, this work highlights the importance of considering the effects of galvanic corrosion on the stability of multicomponent nanoparticles, and it shows how mass transport in a nanoscale system is influenced by redox processes.

1. Introduction

Corrosion results in ~$2.5 trillion of annual financial loss worldwide, representing a significant fraction of the global gross domestic product (GDP).[1] The corrosion of metals is frequently observed under humid atmospheric conditions or in aqueous systems and is accelerated when metal parts are operated at elevated temperatures or in contact with electrolytes. When two metals with different electrochemical potentials form a junction, a process called galvanic or bimetallic corrosion occurs, where the more active metal (i.e., higher oxidation potential or lower electrode potential) is preferentially etched before corrosion of the less active one occurs.[2] In such a situation, the two metals form a galvanic couple, and the electric current flow between the two accelerates the corrosion of the more active metal (**Scheme 1**). Galvanic corrosion is also responsible for many local corrosion and pitting processes in multi-phase and micro-segregating alloys;[3-5] however, it is not always detrimental as the corrosion of the more active metal species can protect the other component. For example, aluminum- and zinc-based coatings and blocks have been widely used to protect structural steel used in the marine, automobile, and construction industries through sacrificial galvanic corrosion.[6-8]

This article is protected by copyright. All rights reserved.

16163028, 2021, 46, Downloaded from https://onlinelibrary.wiley.com/doi/10.1002/adfm.202105866 by Office Of Scientific And Technical Information, Wiley Online Library on [30/08/2023]. See the Terms and Conditions (https://onlinelibrary.wiley.com/terms-and-conditions) on Wiley Online Library for rules of use; OA articles are governed by the applicable Creative Commons License

Author Manuscript

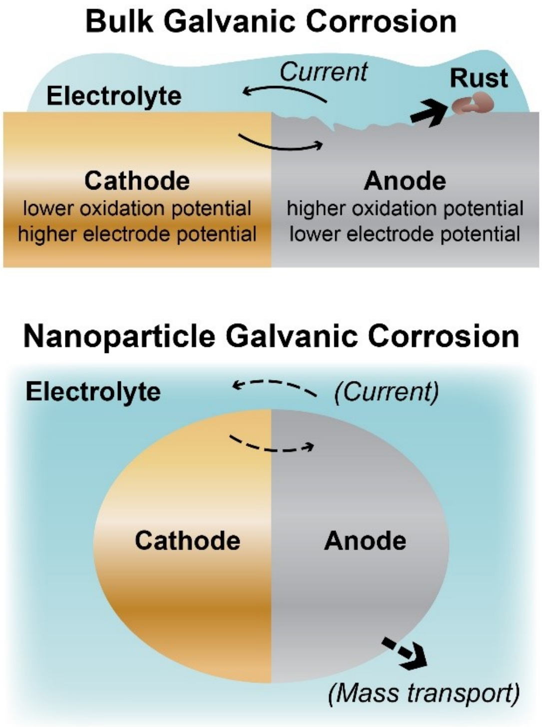

Scheme 1. Galvanic corrosion (a.k.a. bimetallic corrosion) of dissimilar materials in bulk materials and NPs.

Recently, functional metallic nanoparticles (NPs) have become increasingly complex in terms of both composition and domain/interface configuration[9, 10] in efforts to address performance needs for electrocatalysis, biomolecular sensing, and therapeutic applications.[11-13] In principle, these nanostructures should follow the same electrochemical rules as their bulk counterparts and will therefore suffer corrosion in their operating environments, which can consist of strong electrolytes and/or humid atmospheres.[14, 15] However, the behavior and dynamics of the corrosive degradation of NPs, especially heterostructured NPs, have not been systematically studied. This is due, in part, to a lack of reliable methods to generate heterojunction NPs composed of chemically distinct metal domains as well as the inadequacy of compatible techniques to monitor their nanoscale transformations.[16, 17] While the dissolution dynamics of only a few types of noble metal and core-shell NPs (Pd, Pt, and Au) have been observed using conventional liquid-cell transmission

This article is protected by copyright. All rights reserved.

16163028, 2021, 46, Downloaded from https://onlinelibrary.wiley.com/doi/10.1002/adfm.202105866 by Office Of Scientific And Technical Information, Wiley Online Library on [30/08/2023]. See the Terms and Conditions (https://onlinelibrary.wiley.com/terms-and-conditions) on Wiley Online Library for rules of use; OA articles are governed by the applicable Creative Commons License

16163028, 2021, 46, Downloaded from https://onlinelibrary.wiley.com/doi/10.1002/adfm.202105866 by Office Of Scientific And Technical Information, Wiley Online Library on [30/08/2023]. See the Terms and Conditions (https://onlinelibrary.wiley.com/terms-and-conditions) on Wiley Online Library for rules of use; OA articles are governed by the applicable Creative Commons License

Author Manuscript

electron microscopy (TEM),[18-24] a new set of integrated tools capable of both synthesizing heterostructured NPs and studying their corrosion dynamics need to be developed.

2. Results and Discussion

Herein, we systematically investigate the corrosion of heterostructured NPs through a combination of *ex situ* and *in situ* electron microscopy techniques. Scanning probe block copolymer lithography (SPBCL) was used to synthesize bimetallic NPs consisting of one noble metal (e.g., Au and Ag) and one non-noble metal (e.g., Co, Ni, and Cu) on electron-transparent substrates.[25] Via this method, a block copolymer poly(ethylene oxide)-*block*-poly(2-vinylpyridine) (PEO-*b*-P2VP) was dissolved in water and mixed with metal precursors ($HAuCl_4$ for Au, and metal nitrates for all others) to form an ink. This ink was dip-coated onto a scanning probe cantilever and then patterned onto silicon nitride membranes (thickness: 15 or 50 nm) to form dome-shaped nanoreactor arrays. These samples were thermally treated in a hydrogen atmosphere at up to 500 °C (see Methods), which resulted in the formation of an individual NP in each nanoreactor. As the composition is governed by the ratio of metal precursors in the ink, the resulting NPs were either pure metallic, homogeneous alloy, or heterostructured NPs. These structures were then used to study NP corrosion behavior in aqueous environments.

When bimetallic NPs were immersed in aqueous liquids and then examined by scanning transmission electron microscopy (STEM), we found that their electrochemical stability was dependent on the elemental combinations and the liquids used (**Figure 1**A). Au-Cu forms uniform alloy NPs, and after being treated with either a 0.5 M KCl or 0.5 M HCl solution for 1 h, no significant change in the Au and Cu spatial distribution was observed (Figure 1B). Quantitative energy-dispersive X-ray spectroscopy (EDS) reveals that the atomic fraction of Au increases from ~59% to ~68% and ~70% after immersion in KCl and HCl, respectively (Figure 1C). In contrast, pure Cu NPs

This article is protected by copyright. All rights reserved.

readily dissolve in acidic solution. To create a junction structure, we replaced the Cu with Co, since it has a large miscibility gap with Au (Figure 1E). With these Au-Co NPs, the Co domain was completely etched after 1 h in a 0.5 M KCl solution (Figure 1F and S1), as Co has a higher oxidation potential than Au, leaving half-spheroid Au NPs. This type of asymmetric particle shape is thermodynamically unfavored, as it consists of a half-spheroid and with a flat or even concave surface originating from the bimetallic interface present before etching.[26-28] As such, galvanic corrosion provides a viable way of synthesizing non-equilibrium NPs, which are difficult to prepare via colloidal and solid-state syntheses.

Author Manuscript

This article is protected by copyright. All rights reserved.

16163028, 2021, 46, Downloaded from https://onlinelibrary.wiley.com/doi/10.1002/adfm.202105866 by Office Of Scientific And Technical Information, Wiley Online Library on [30/08/2023]. See the Terms and Conditions (https://onlinelibrary.wiley.com/terms-and-conditions) on Wiley Online Library for rules of use; OA articles are governed by the applicable Creative Commons License

Author Manuscript

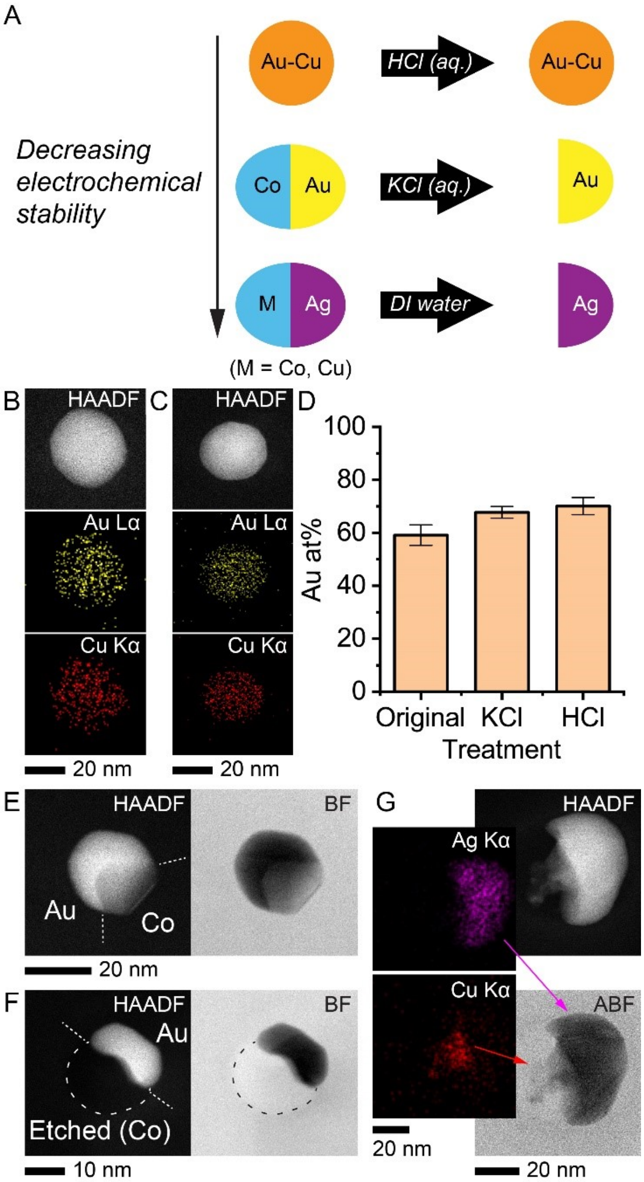

Figure 1. *Ex situ* corrosion of bimetallic NPs in aqueous environments. (A) Schematic showing the corrosion products of different bimetallic NPs in various liquids. (B, C) High-angle annular dark-field (HAADF) images and energy-dispersive X-ray spectroscopy (EDS) maps of two Au-Cu NPs in their original state (B) and after exposure to 0.5 M HCl for 1 h (C). (D) Plot of the Au atomic fraction, as determined by EDS, for Au-Cu NPs in their original state and after exposure to 0.5 M KCl or 0.5 M HCl for 1 h. Error bars represent the standard deviation of 5 consecutive and adjacent NPs in an array. (E, F) HAADF and bright-field (BF) images of two Au-Co NPs in their original state (E) and after exposure to DI water for 2.5 h (F). (G) HAADF and annular bright-field (ABF) images of a Ag-Cu NP exposed to DI water for 2.5 h that contain Cu residues. EDS maps (insets) correspond to the Ag and Cu-containing domains.

Similar selective etching was observed for Ag-M NPs (M = Co, Ni, and Cu). However, since Ag ions readily form AgCl in aqueous KCl solutions, the subsequent dissolution of the Ag from the NPs

This article is protected by copyright. All rights reserved.

16163028, 2021, 46, Downloaded from https://onlinelibrary.wiley.com/doi/10.1002/adfm.202105866 by Office Of Scientific And Technical Information, Wiley Online Library on [30/08/2023]. See the Terms and Conditions (https://onlinelibrary.wiley.com/terms-and-conditions) on Wiley Online Library for rules of use; OA articles are governed by the applicable Creative Commons License

16163028, 2021, 46, Downloaded from https://onlinelibrary.wiley.com/doi/10.1002/adfm.202105866 by Office Of Scientific And Technical Information, Wiley Online Library on [30/08/2023]. See the Terms and Conditions (https://onlinelibrary.wiley.com/terms-and-conditions) on Wiley Online Library for rules of use; OA articles are governed by the applicable Creative Commons License

Author Manuscript

was rapid, and the Ag-M NPs were completely etched within 1 h. To preserve the Ag portion, Ag-containing NPs were immersed in deionized (DI) water for 2.5 h and then examined using STEM. As the corrosion of Ag is both initiated and dominated by trace sulfuric species present in the atmosphere,[29-31] we first examined the fate of pure Ag NPs under these conditions. As expected, STEM images and EDS elemental maps suggest that the oxidation products of Ag NPs consist of Ag and S (Figure S2 and S3). However, when heterostructured Ag-Co and Ag-Cu NPs were immersed in DI water for 2.5 h, the more active transition metal was selectively etched, while the Ag domain remained intact (Figure S4 and S5). In a few (<10%) of the larger Ag-Cu NPs, some Cu-containing species are present, as shown by EDS elemental maps (Figure 1G). Here, the Ag hemisphere shows distinct geometry and contrast from the Cu-containing parts, and no significant O or S enrichment was observed in the surroundings of the Ag domain (Figure S6). This observation suggests that the Cu sacrificially corrodes and protects the less active metal (Ag), which otherwise corrodes under the same conditions. Accordingly, the Ag serves as the cathode for the reduction of oxygen. In addition, atomic-resolution annular bright-field (ABF) images reveal that the fragmented Cu-containing residues have a tenorite CuO structure (Figure S7A), which is also observed for partially corroded Ag-Cu NPs after 1 h in DI water (Figure S7B). As such, this residue is the oxide that formed through the galvanic corrosion of Cu from the NPs.

A different behavior was observed for Ag-Ni NPs. Although Ni has a higher oxidation potential than Cu, the Ni portion in the Ag-Ni NPs was mostly preserved after a 2.5 h treatment with DI water (Figure S8A and B). Here, a shell is observed on the Ni surface, consisting of various interconnected domains with lower contrast than the core (Figure S8C). According to atomic-resolution ABF, this shell adopts a rock salt NiO structure and appears to have an aligned lattice orientation relationship with the underlying metallic Ni in the core (Figure S8D). The passivation of the Ni with a contiguous NiO shell significantly decreased the corrosion kinetics for Ni.[32, 33] This result suggests that fast-corroding metals, such as Cu, may have a completely different mass

This article is protected by copyright. All rights reserved.

transport behavior than Ni during the corrosion process. We hypothesize that the Cu breakdown during galvanic corrosion in a Ag-Cu NP may be fractal and fragmented, as CuO has a crystal symmetry distinct from metallic Cu, which keeps the oxides from forming a conformal protective layer on the metal surface.

In order to observe the nanoscale corrosion dynamics and mass transport behavior of heterojunction NPs, we implemented an *in situ* liquid-cell transmission electron microscopy platform that is compatible with SPBCL synthesis and capable of real-time monitoring with high spatial and temporal resolution (**Figure 2**A). Here, we patterned arrays of polymer nanoreactors containing Ag and Cu precursors on a silicon nitride membrane immobilized on a silicon chip that forms the top half of a TEM liquid flow cell (Figure S9). This chip was then processed using the standard heat treatment protocols that yield heterostructured Ag-Cu NPs (see Methods).[25] To the other half of the cell, a graphene sheet (3-5 layers thick) was wet-transferred onto the silicon nitride that forms the bottom window;[34] the graphene consumes the electron-induced free radicals formed during imaging (Figure S10).[35, 36] The top and bottom chips with the windows were sandwiched and used to assemble the cell, and DI water was pumped into the system to enable corrosion. *In situ* high-angle annular dark-field (HAADF) imaging in a STEM was performed to identify the Ag, Cu, and the oxidation products in real time as they have distinct mass densities. However, strong electron scattering by the thick water layer (typically a few hundred nm)[37] prevents video-rate HAADF imaging of these 20-50 nm NPs (Figure S11). To enable high-resolution, video-rate monitoring via STEM, a gas bubble inside the liquid cell was generated to reduce the thickness of the water layer in the electron beam path (Figure 2B). Here, an air bubble was produced by slowly injecting water into the air-filled liquid cell. In addition, extra gas (usually H_2 and O_2 from water radiolysis) is generated when the electron beam interacts with water, such that the bubble becomes stable and is size-tunable.[38] In this configuration, the thin water layer between the bubble and silicon nitride membrane, proven to exist by earlier studies,[38] enables radical-induced corrosion of the NPs. The

This article is protected by copyright. All rights reserved.

Author Manuscript

16163028, 2021, 46, Downloaded from https://onlinelibrary.wiley.com/doi/10.1002/adfm.202105866 by Office Of Scientific And Technical Information, Wiley Online Library on [30/08/2023]. See the Terms and Conditions (https://onlinelibrary.wiley.com/terms-and-conditions) on Wiley Online Library for rules of use; OA articles are governed by the applicable Creative Commons License

presence of radicals, most notably H• and OH•,[39] significantly accelerates the corrosion dynamics compared to the reaction under ambient conditions and is therefore suitable for *in situ* electron microscopy.

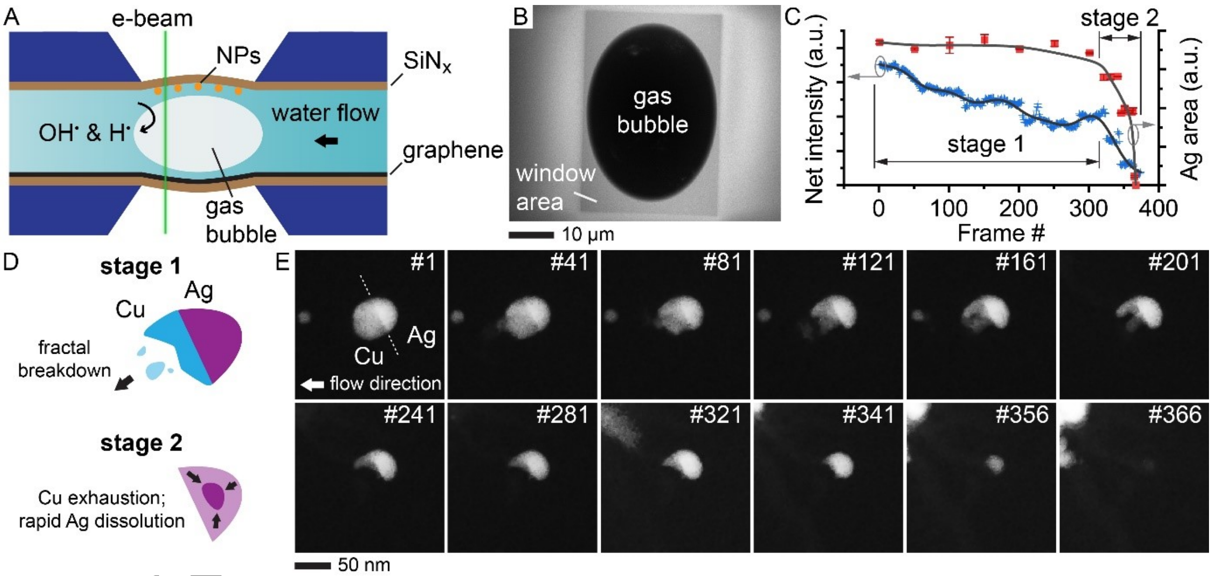

Figure 2. Aqueous radical-induced NP corrosion in liquid-cell STEM. (A) Schematic of the liquid flow cell for *in situ* observation of NP corrosion. (B) Secondary electron (SE) image of the liquid cell window showing the presence of a gas micro-bubble. (C) Net (background subtracted) HAADF intensity of a Ag-Cu NP (blue) and the area of the Ag portion (red) as a function of frame number from Movie S1. Black curves represent smoothed results. (D) Schematic of the two-stage corrosion behavior. (E) Denoised HAADF frames showing the corrosion of a Ag-Cu NP (extracted from Movie S1). Frame time in Movie S1, ~0.3 s.

The corrosion dynamics of a Ag-Cu NP were recorded in HAADF mode and subsequently denoised (Movie S1, see Methods for details). To study the kinetics of the corrosion process, we first quantified the net HAADF intensity of the entire NP (subtracting the average background level of each frame) as a function of frame number (time). Here, a two-stage process was identified. In the first stage, the net HAADF intensity decreases quasi-linearly with minor fluctuations (Figure 2C), consistent with the fractal breakdown of Cu (Figure 2D). Indeed, consistent with our hypothesis, the Cu does not dissolve gradually but rather breaks apart into small pieces and flows away from the NP

Author Manuscript

This article is protected by copyright. All rights reserved.

16163028, 2021, 46, Downloaded from https://onlinelibrary.wiley.com/doi/10.1002/adfm.202105866 by Office Of Scientific And Technical Information, Wiley Online Library on [30/08/2023]. See the Terms and Conditions (https://onlinelibrary.wiley.com/terms-and-conditions) on Wiley Online Library for rules of use; OA articles are governed by the applicable Creative Commons License

(Figure 2E, first row). Interestingly, Cu etching does not preferentially occur along the Ag-Cu interface to form a groove,[40] consistent with the hypothesis that an electrochemical potential gradient across the interface drives the corrosion process.

A second stage was identified by the fast dissolution of the higher-contrast (brighter) Ag portion. To discern whether the Ag-Cu couple follows a galvanic corrosion pathway or the electron beam effect kinetically dominates, we measured the geometric projection area of the Ag portion in the movie as a function of frame number (Figure 2C). The Ag area does not change significantly during the first stage that was defined by HAADF intensities. However, once the Cu is exhausted at the beginning of the second stage, the Ag rapidly dissolves. This result confirms that only after the Cu is completely sacrificed does the Ag in a junction NP begin to corrode, in agreement with a galvanic corrosion process.

Next, we sought to investigate the corrosion dynamics of Ag-Cu NPs in the vapor phase. As no liquid flow is involved in this experimental configuration, oxidation products may deposit around a NP, and the corrosion dynamics can be used to validate the liquid-phase results. An *in situ* gas flow sample holder was used to provide an almost pure water steam environment at a controlled pressure, which allowed for the radical-accelerated corrosion of NPs in the vapor phase to be studied in an electron microscope (**Figure 3**A). This setup is like that used for the gas-phase oxidation of alloy nanoparticles reported in the literature,[41-45] but the current experiment uses water vapor instead of oxygen or air. Here, polymer nanoreactors were patterned on the upper window chip (Figure 3B) and thermally converted into Ag-Cu NP arrays (Figure 3C). After the gas flow cell was assembled, a liquid container system was filled with DI water and connected to the pumping system of the sample holder with the inlet valve closed. The holder was evacuated before the valve was opened to introduce water vapor into the system and allowed to equilibrate at 13–14 Torr. Here, the corrosion of NPs was induced by increasing the electron dose rate (see Methods for detailed

This article is protected by copyright. All rights reserved.

Author Manuscript

16163028, 2021, 46, Downloaded from https://onlinelibrary.wiley.com/doi/10.1002/adfm.202105866 by Office Of Scientific And Technical Information, Wiley Online Library on [30/08/2023]. See the Terms and Conditions (https://onlinelibrary.wiley.com/terms-and-conditions) on Wiley Online Library for rules of use; OA articles are governed by the applicable Creative Commons License

conditions) in STEM mode, and sequential HAADF images were recorded as a movie (Movie S2). The corrosion of a Ag-Cu NP occurred via a two-stage process similar to that observed in the liquid cell (Figure 3D). During the first ~19 s, the Cu portion (lower contrast) corroded into fractal materials under electron irradiation. After the Cu was fully consumed, the remaining Ag section was rapidly oxidized, and this residue was deposited around the NP (Figure S12) due to the lack of liquid flow. Like the liquid-phase results, Cu etching during the first stage shows quasi-linear behavior (Figure S13), suggesting that it has a persistent and relatively non-changing reaction rate coefficient. In contrast, Ag etching is initially slow but gradually accelerates (in the first few seconds) as the Cu content decreases. These results suggest that the galvanic corrosion of NPs can occur in a water vapor environment, even though no liquid was apparent. This is in contrast to the bulk phase, where condensed liquids are typically necessary for atmospheric corrosion to occur, as ion migration in a liquid electrolyte is necessary to complete the circuit. However, for supported NPs, diffusion of atoms along the surface of NPs and the substrate is typically multiple orders of magnitude faster than bulk diffusion,[46, 47] and the required diffusion length is on the order of a few to tens of nanometers. As a result, an electrochemical loop may form between the two metals and the surrounding supportive materials (similar to miniaturized solid-state electrolytes).

Author Manuscript

This article is protected by copyright. All rights reserved.

16163028, 2021, 46, Downloaded from https://onlinelibrary.wiley.com/doi/10.1002/adfm.202105866 by Office Of Scientific And Technical Information, Wiley Online Library on [30/08/2023]. See the Terms and Conditions (https://onlinelibrary.wiley.com/terms-and-conditions) on Wiley Online Library for rules of use; OA articles are governed by the applicable Creative Commons License

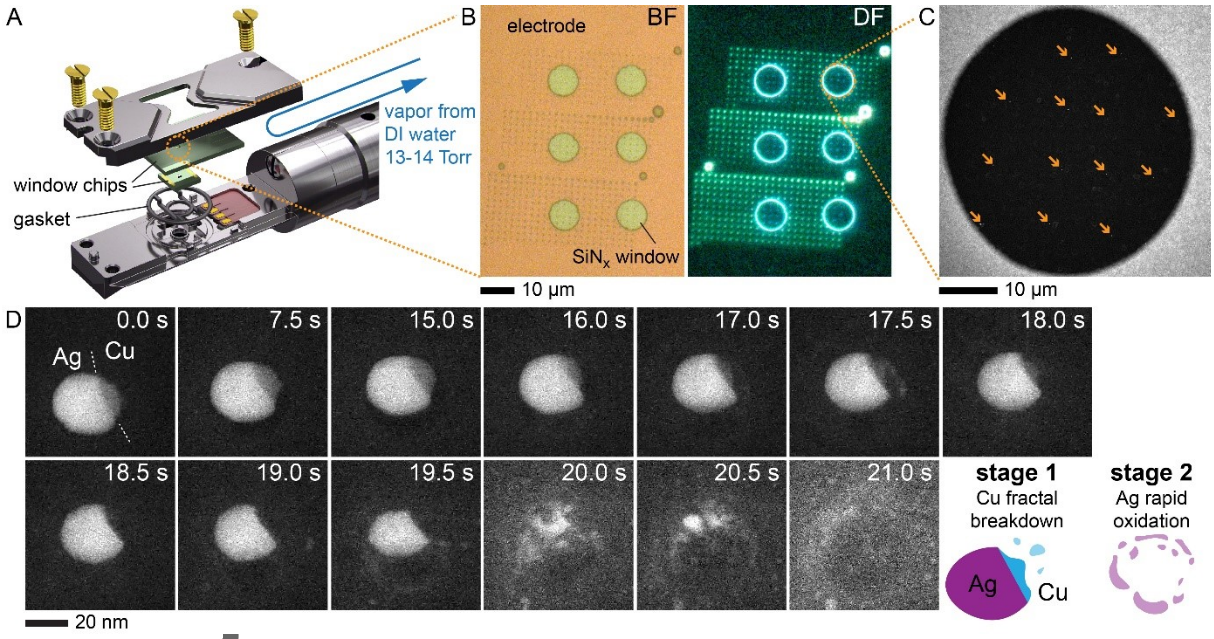

Figure 3. Vapor-phase radical-induced NP corrosion in gas-cell STEM. (A) Illustration of the gas-cell *in situ* TEM holder. Adapted image courtesy of Protochips, Inc. (B) Optical BF and dark-field (DF) microscopy images of the window area patterned with polymer nanoreactors (dot arrays; on the inner side of the chip). (C) HAADF image of one silicon nitride window patterned with arrays of Ag-Cu NPs (arrows point to individual NPs). (D) Denoised HAADF frames showing the corrosion of a Ag-Cu NP (extracted from Movie S2) following a two-stage corrosion process.

Finally, we investigated potential ways to hinder the galvanic corrosion process and enhance the stability of hetero-bimetallic NPs. Surface cleaning using Ar plasma is typically considered to be a non-oxidative etching process that removes surface contamination and oxide layers.[48] Surprisingly, we discovered that Ag-Cu NPs treated with a mild Ar plasma (90 mTorr, 45 W, 2 min) have significantly enhanced stability against galvanic corrosion. As discussed above, the Cu portion in almost all (> 90%) as-synthesized Ag-Cu NPs has corroded after immersion in DI water for 2.5 h (**Figure 4**A). In contrast, ~ 60% of Ar plasma-treated Ag-Cu NPs remained intact under the same conditions, and the remaining NPs exhibited only partial Cu corrosion (Figure 4B). To investigate this, we looked at the Ag-Cu interface in a plasma-treated NP, where we observed that the Cu surface is coated with a shell layer (Figure 4E). Line profiles of the HAADF intensity across the Ag and Cu surfaces confirm that an ~1.9 nm thick surface layer exists on the Cu side, while the Ag surface is

Author Manuscript

This article is protected by copyright. All rights reserved.

16163028, 2021, 46, Downloaded from https://onlinelibrary.wiley.com/doi/10.1002/adfm.202105866 by Office Of Scientific And Technical Information, Wiley Online Library on [30/08/2023]. See the Terms and Conditions (https://onlinelibrary.wiley.com/terms-and-conditions) on Wiley Online Library for rules of use; OA articles are governed by the applicable Creative Commons License

bare (Figure 4F). ABF imaging was used to reveal the lattice structure of this layer, and the Fourier transform of the surface region suggests that it has a tenorite CuO structure (Figure 4G). This observation is in contrast to the surface structure of as-synthesized Ag-Cu NPs in which a thin, amorphous oxide layer exists on the Cu surface (Figure S14). After the Ar plasma treatment, the bulk Cu part is still metallic, as suggested by electron energy-loss spectroscopy (EELS), and only the surface structure is modified (Figure S15).

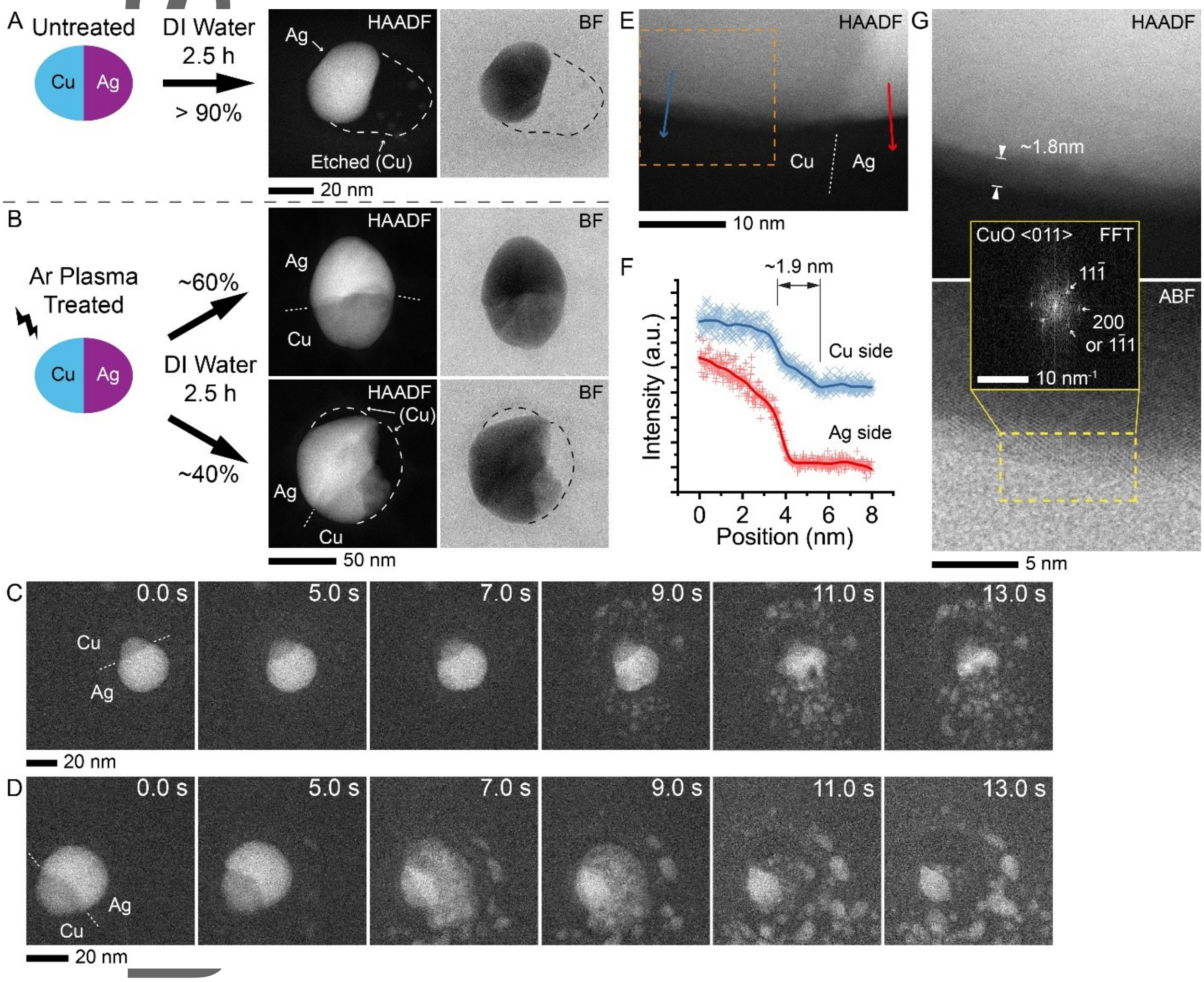

Figure 4. Influence of surface structure on the corrosion of Ag-Cu NPs. (A, B) Schematic and microscopy images of the corrosion products of untreated (A) and Ar plasma-treated (B) Ag-Cu NPs. (C, D) HAADF frames showing the corrosion of two Ag-Cu NPs after Ar plasma treatment (extracted from Movie S3 and S4, respectively) reveal no sacrificial corrosion of Cu. (E) HAADF image of the surface of a Ag-Cu NP after Ar plasma treatment. (F) Line profile of the HAADF intensity across the Ag (red) and Cu (blue) surfaces in (E). Crosses and solid curves represent original and smoothed data,

This article is protected by copyright. All rights reserved.

16163028, 2021, 46, Downloaded from https://onlinelibrary.wiley.com/doi/10.1002/adfm.202105866 by Office Of Scientific And Technical Information, Wiley Online Library on [30/08/2023]. See the Terms and Conditions (https://onlinelibrary.wiley.com/terms-and-conditions) on Wiley Online Library for rules of use; OA articles are governed by the applicable Creative Commons License

respectively. (G) HAADF and ABF images from the dashed box region in (E) showing the existence of a dense oxide layer on the Cu surface. Inset: Fast Fourier transform (FFT) of the oxide region from the ABF image (yellow dashed box).

Based on the atomic-resolution STEM data, we hypothesize that a mild Ar plasma treatment converts the amorphous oxide on the Cu surface into a dense, crystalline CuO shell through particle collision.[49, 50] The introduction of such an oxide shell insulates the metallic Cu from electrolytes, thereby hindering electrochemical galvanic corrosion.[51, 52] To validate this hypothesis, we annealed plasma-treated NPs in H_2 to reduce the oxide back to the metallic state[53] (see Methods for detailed conditions) and then immersed the samples in DI water for 2.5 h. Here, the pure Ag NPs showed a similar sulfur-directed corrosion behavior as the untreated ones (Figure S16), and the Ag-Cu heterostructured NPs lost their plasma-induced stability against galvanic corrosion (Figure S17). These results confirm that the surface oxide on Cu, rather than the deposition or removal of other materials (e.g., hydrocarbons), is responsible for the plasma-induced stability.

The Ar plasma-treated NPs show a surprising vapor-phase corrosion behavior when examined by *in situ* STEM (Movie S3 and S4). Here, the Ag corrodes prior to the Cu, even though Ag has a significantly lower oxidation potential (Figure 4C and D). Since the Cu surface is passivated by an oxide shell, the current flow required for galvanic corrosion is suppressed; thus, the bare Ag surface corrodes faster than the CuO surface. As such, the controlled generation of a dense, crystalline oxide shell by Ar plasma may offer a practical approach to enhance NP stability against galvanic corrosion as it does not significantly modify the NP geometry or elemental distribution.

3. Conclusion

In conclusion, we have shown that heterobimetallic NPs, which consist of metals with different electrochemical potentials, undergo a galvanic corrosion process similar to their bulk

This article is protected by copyright. All rights reserved.

Author Manuscript

16163028, 2021, 46, Downloaded from https://onlinelibrary.wiley.com/doi/10.1002/adfm.202105866 by Office Of Scientific And Technical Information, Wiley Online Library on [30/08/2023]. See the Terms and Conditions (https://onlinelibrary.wiley.com/terms-and-conditions) on Wiley Online Library for rules of use; OA articles are governed by the applicable Creative Commons License

counterparts when exposed to aqueous environments. Importantly, one can no longer assume the stability of a multicomponent NP based on the stability of its constituent elements alone but rather a consideration of their collective interactions. The galvanic corrosion phenomenon reported herein is likely important in many situations where NPs are in contact with concentrated electrolyte solutions, for example, during electrocatalysis and in a biological milieu (therapeutics and probes).

Although this study is a significant advance in observing and understanding the galvanic corrosion of heterojunction NPs comprising non-noble metals, we do note that the electron beam inevitably plays a role in the *in situ* corrosion experiments. As electron microscopy instrumentation evolves, these beam effects may be minimized in future studies. Finally, since massive libraries of multimetallic NPs with distinct phase structures and interfacial configurations can be synthesized using SPBCL,[9, 25] this work will not only open avenues for further nanoscale corrosion studies but also high-throughput approaches to screen and understand the electrochemical stability and corrosion behavior of multimetallic systems in general.

4. Methods

Materials and Chemicals: Chloroauric acid hydrate ($HAuCl_4 \cdot xH_2O$, ≥99.9% trace metals basis), silver nitrate ($AgNO_3$, anhydrous, ≥99.999% trace metals basis), copper(II) nitrate hydrate [$Cu(NO_3)_2 \cdot xH_2O$, 99.999%], cobalt(II) nitrate hexahydrate [$Co(NO_3)_2 \cdot 6H_2O$, 99.999%], nickel(II) nitrate hexahydrate [$Ni(NO_3)_2 \cdot 6H_2O$, 99.999%], nitric acid (HNO_3, 70%, redistilled, ≥99.999% trace metals basis), hexamethyldisilazane (HMDS, 99.9%), and hexane (anhydrous, 95%) were purchased from Sigma-Aldrich. Poly(ethylene oxide)-*block*-poly(2-vinylpyridine) (PEO-*b*-P2VP, M_n = 2.8-*b*-1.5 kg·mol^{-1}, polydispersity index = 1.11) was purchased from Polymer Source, Inc. Dip-Pen Nanolithography (DPN) 1D pen arrays (type M, without a gold coating) were purchased from Advanced Creative Solutions Technology, LLC. Silicon nitride membranes for TEM (amorphous, thickness = 15 nm) were

This article is protected by copyright. All rights reserved.

Author Manuscript

16163028, 2021, 46, Downloaded from https://onlinelibrary.wiley.com/doi/10.1002/adfm.202105866 by Office Of Scientific And Technical Information, Wiley Online Library on [30/08/2023]. See the Terms and Conditions (https://onlinelibrary.wiley.com/terms-and-conditions) on Wiley Online Library for rules of use; OA articles are governed by the applicable Creative Commons License

Author Manuscript

purchased from Ted Pella, Inc. Liquid-cell and gas-cell window chips were purchased from Protochips, Inc. Chemical vapor deposition (CVD) graphene (3–5 layers) supported on copper foil was purchased from ACS Material, LLC.

Synthesis of NPs: Silicon nitride membranes or window chips (for liquid and gas cells) were hydrophobically modified with HMDS by vapor deposition. The membranes were placed into a closed chamber with vials containing a HMDS/hexane mixture (volume ratio 1:1) and kept overnight at room temperature. PEO-*b*-P2VP and metal precursors were dissolved in deionized water with deliberately varied molar ratios of metal species to form an ink solution. The resulting solution had a polymer concentration of 5 mg·mL^{-1} and a 32:1 molar ratio of pyridyl groups to total metal species. Inks were acidified by adding HNO_3 (0.1 M aqueous solution) at a volume ratio of 2 μL per 1 mL and stirred overnight at room temperature prior to use. After the inking process, the pen arrays were mounted onto an AFM (Park Systems XE-150) in a chamber with a temperature of 20 °C and relative humidity of 76%. Arrays of polymer nanoreactors were deposited by bringing the pen arrays in contact with the silicon nitride membranes. The samples were thermally treated in a tube furnace under a hydrogen atmosphere as follows: ramped to 150 °C at 2.1 °C·min^{-1}; ramped to 240 °C at 0.25 °C·min^{-1} and kept thermostatic for 18 h; ramped to 500 °C at 4.3 °C·min^{-1} and kept thermostatic for 12 h; cooled to room temperature under ambient conditions.

Ar plasma treatment: Samples were placed in the vacuum chamber of a South Bay Technology PC2000 plasma cleaner. After pumping down for ~5 min, Ar gas was flowed into the chamber to reach an equilibrium pressure of 90 mTorr. Plasma treatment was performed at a power of 45 W for 2 min.

This article is protected by copyright. All rights reserved.

16163028, 2021, 46, Downloaded from https://onlinelibrary.wiley.com/doi/10.1002/adfm.202105866 by Office Of Scientific And Technical Information, Wiley Online Library on [30/08/2023]. See the Terms and Conditions (https://onlinelibrary.wiley.com/terms-and-conditions) on Wiley Online Library for rules of use; OA articles are governed by the applicable Creative Commons License

16163028, 2021, 46, Downloaded from https://onlinelibrary.wiley.com/doi/10.1002/adfm.202105866 by Office Of Scientific And Technical Information, Wiley Online Library on [30/08/2023]. See the Terms and Conditions (https://onlinelibrary.wiley.com/terms-and-conditions) on Wiley Online Library for rules of use; OA articles are governed by the applicable Creative Commons License

Author Manuscript

Reduction of plasma-treated NPs: To reduce the NPs treated by Ar plasma, the NP samples were thermally annealed in a tube furnace under a hydrogen atmosphere as follows: ramped to 500 °C at 8 °C·min^{-1} and kept thermostatic for 12 h; cooled to room temperature under ambient conditions.

In situ liquid-cell STEM: A Protochips Poseidon liquid-cell holder (Hitachi interface) was used. Before cell assembly, a 3-5 layer CVD graphene sheet was transferred to the bottom window chip following literature protocols,[34] and NP arrays were patterned on the top window chip. The top and bottom chips were then assembled into the liquid cell in the dry state. The liquid-cell holder was transferred into a Hitachi HD-2300A equipped with a field-emission gun (FEG) operated at 200 kV for *in situ* STEM imaging in HAADF and secondary electron (SE) modes. DI water was pumped into the liquid cell at a rate of ~2 µL·min^{-1}. A gas bubble within the water flow was generated and maintained under the electron beam. *In situ* HAADF movies were recorded at a resolution of 512 × 512 px, scan area of 207.17 × 207.17 nm, and pixel dwell time of 1 µs (Movie S1). The probe current was 0.168 nA. HAADF movies were denoised following a published protocol[54] using the video block-matching and 3D filtering (V-BM3D) method.[55]

In situ gas-cell STEM: A Protochips Atmosphere gas-cell holder (JEOL interface) was used. A top window chip carrying NP arrays was assembled with a bottom chip to form a gas cell. The gas-cell holder was transferred into a JEOL JEM-ARM200CF equipped with a cold FEG operated at 200 kV and a CEOS hexapole probe aberration corrector. This microscope was used for *in situ* STEM imaging in HAADF mode. A Protochips water vapor kit was connected to the pumping system of the holder and filled with DI water. After the pipeline and the holder were pumped down, the valve on the water

This article is protected by copyright. All rights reserved.

vapor kit was opened to let the water vaporize in the high vacuum. The pressure inside the system was allowed to equilibrate at 13–14 Torr before imaging. *In situ* HAADF movies were recorded at a resolution of 512 × 512 px, scan area of 93.1 × 93.1 nm (Movie S2 and S3) or 124.17 × 124.17 nm (Movie S4), and pixel dwell time of 0.8 µs. The probe current was 0.069 nA.

Ex situ STEM: A JEOL JEM-2100F equipped with a FEG was operated at 200 kV for HAADF imaging. The JEOL JEM-ARM200CF and a GrandARM300F carrying a cold FEG operated at 300 kV were used for HAADF and bright-field (BF) imaging and EDS. All EDS characterization was performed on a JEOL beryllium holder to minimize background signals. EDS quantification was performed in Oxford Instruments AZtec based on factory standardizations; the quantification uncertainty was always < 2 wt%, as determined by the Aztec software. Atomic-resolution imaging was performed on the JEOL JEM-ARM200CF with a convergence angle of 27.5 mrad, and a collection angle of 90−370 mrad (HAADF) or 10−23 mrad (ABF). Electron energy-loss spectroscopy (EELS) was performed on the JEOL JEM-ARM200CF with a Gatan Quantum Dual EELS system. Convergence angle: 27.5 mrad; collection angle: 37 mrad.

Supporting Information

Supporting Information is available from the Wiley Online Library or from the author.

Acknowledgements

The authors thank Sara M. Rupich (Northwestern University) for helpful discussions. The *in situ* gas system was supported by Protochips Inc. This material is based upon work supported by the Sherman Fairchild Foundation, Inc. (for synthesis and electron microscopy), the Air Force Office of Scientific Research award FA9550-17-1-0348 (for electron microscopy), and the Center for Bio-Inspired Energy Science, an Energy Frontier Research Center funded by the U.S. Department of Energy, Office of Science, Basic Energy Sciences award DE-SC0000989 (for synthesis). This work made use of the EPIC facility of Northwestern University's NUANCE Center, which has received support from the SHyNE Resource (NSF ECCS-2025633), the IIN, and Northwestern's MRSEC program (NSF DMR-1720139).

This article is protected by copyright. All rights reserved.

Author Manuscript

16163028, 2021, 46, Downloaded from https://onlinelibrary.wiley.com/doi/10.1002/adfm.202105866 by Office Of Scientific And Technical Information, Wiley Online Library on [30/08/2023]. See the Terms and Conditions (https://onlinelibrary.wiley.com/terms-and-conditions) on Wiley Online Library for rules of use; OA articles are governed by the applicable Creative Commons License

Received: ((will be filled in by the editorial staff))
Revised: ((will be filled in by the editorial staff))
Published online: ((will be filled in by the editorial staff))

References

[1] G. Koch, J. Varney, N. Thompson, O. Moghissi, M. Gould, J. Payer, (Ed: G. Jacobson), NACE International, Houston, TX 2016.

[2] B. N. Popov, in *Corrosion Engineering*, (Ed: B. N. Popov), Elsevier, Amsterdam 2015, 239.

[3] C. T. Kwok, S. L. Fong, F. T. Cheng, H. C. Man, *J. Mater. Process. Technol.* **2006**, *176*, 168.

[4] C.-M. Liao, R. P. Wei, *Electrochim. Acta* **1999**, *45*, 881.

[5] J. Idrac, G. Mankowski, G. Thompson, P. Skeldon, Y. Kihn, C. Blanc, *Electrochim. Acta* **2007**, *52*, 7626.

[6] X. G. Zhang, *J. Electrochem. Soc.* **1996**, *143*, 1472.

[7] M. C. Reboul, *Corrosion* **2013**, *35*, 423.

[8] A. Farooq, M. Hamza, Q. Ahmed, K. M. Deen, *Electrochim. Acta* **2019**, *314*, 135.

[9] P.-C. Chen, M. Liu, J. S. Du, B. Meckes, S. Wang, H. Lin, V. P. Dravid, C. Wolverton, C. A. Mirkin, *Science* **2019**, *363*, 959.

[10] Y. Yao, Z. Huang, P. Xie, S. D. Lacey, R. J. Jacob, H. Xie, F. Chen, A. Nie, T. Pu, M. Rehwoldt, D. Yu, M. R. Zachariah, C. Wang, R. Shahbazian-Yassar, J. Li, L. Hu, *Science* **2018**, *359*, 1489.

[11] M. Luo, S. Guo, *Nat. Rev. Mater.* **2017**, *2*, 17059.

[12] T. Löffler, A. Savan, A. Garzón-Manjón, M. Meischein, C. Scheu, A. Ludwig, W. Schuhmann, *ACS Energy Letters* **2019**, 1206.

[13] W.-T. Koo, J. E. Millstone, P. S. Weiss, I.-D. Kim, *ACS Nano* **2020**.

[14] H.-H. Jeong, M. Alarcón-Correa, A. G. Mark, K. Son, T.-C. Lee, P. Fischer, *Adv. Sci.* **2017**, *4*, 1700234.

[15] J. L. Elechiguerra, L. Larios-Lopez, C. Liu, D. Garcia-Gutierrez, A. Camacho-Bragado, M. J. Yacaman, *Chem. Mater.* **2005**, *17*, 6042.

[16] S. W. Chee, M. G. Burke, in *Liquid Cell Electron Microscopy*, (Ed: F. M. Ross), Cambridge University Press, Cambridge 2016, 258.

[17] Z. Song, Z.-H. Xie, *Micron* **2018**, *112*, 69.

[18] Y. Jiang, G. Zhu, F. Lin, H. Zhang, C. Jin, J. Yuan, D. Yang, Z. Zhang, *Nano Lett.* **2014**, *14*, 3761.

This article is protected by copyright. All rights reserved.

16163028, 2021, 46, Downloaded from https://onlinelibrary.wiley.com/doi/10.1002/adfm.202105866 by Office Of Scientific And Technical Information, Wiley Online Library on [30/08/2023]. See the Terms and Conditions (https://onlinelibrary.wiley.com/terms-and-conditions) on Wiley Online Library for rules of use; OA articles are governed by the applicable Creative Commons License

Author Manuscript

16163028, 2021, 46, Downloaded from https://onlinelibrary.wiley.com/doi/10.1002/adfm.202105866 by Office Of Scientific And Technical Information, Wiley Online Library on [30/08/2023]. See the Terms and Conditions (https://onlinelibrary.wiley.com/terms-and-conditions) on Wiley Online Library for rules of use; OA articles are governed by the applicable Creative Commons License

Author Manuscript

[19] X. Ye, M. R. Jones, L. B. Frechette, Q. Chen, A. S. Powers, P. Ercius, G. Dunn, G. M. Rotskoff, S. C. Nguyen, V. P. Adiga, A. Zettl, E. Rabani, P. L. Geissler, A. P. Alivisatos, *Science* **2016**, *354*, 874.

[20] J. Wu, W. Gao, H. Yang, J.-M. Zuo, *ACS Nano* **2017**, *11*, 1696.

[21] H. Shan, W. Gao, Y. Xiong, F. Shi, Y. Yan, Y. Ma, W. Shang, P. Tao, C. Song, T. Deng, H. Zhang, D. Yang, X. Pan, J. Wu, *Nat. Commun.* **2018**, *9*, 1011.

[22] M. R. Hauwiller, L. B. Frechette, M. R. Jones, J. C. Ondry, G. M. Rotskoff, P. Geissler, A. P. Alivisatos, *Nano Lett.* **2018**, *18*, 5731.

[23] M. R. Hauwiller, J. C. Ondry, C. M. Chan, P. Khandekar, J. Yu, A. P. Alivisatos, *J. Am. Chem. Soc.* **2019**, *141*, 4428.

[24] L. Chen, A. Leonardi, J. Chen, M. Cao, N. Li, D. Su, Q. Zhang, M. Engel, X. Ye, *Nat. Commun.* **2020**, *11*, 3041.

[25] P.-C. Chen, X. Liu, J. L. Hedrick, Z. Xie, S. Wang, Q.-Y. Lin, M. C. Hersam, V. P. Dravid, C. A. Mirkin, *Science* **2016**, *352*, 1565.

[26] M. Schnedlitz, R. Fernandez-Perea, D. Knez, M. Lasserus, A. Schiffmann, F. Hofer, A. W. Hauser, M. P. de Lara-Castells, W. E. Ernst, *J. Phys. Chem. C* **2019**, *123*, 20037.

[27] L. Tang, W. Wu, L. He, K. Yu, T. Xu, Q. Zhang, L. Zhang, L. Sun, *J. Phys. Chem. Lett.* **2019**, *10*, 1973.

[28] W. T. Osowiecki, X. Ye, P. Satish, K. C. Bustillo, E. L. Clark, A. P. Alivisatos, *J. Am. Chem. Soc.* **2018**.

[29] C. Kleber, R. Wiesinger, J. Schnöller, U. Hilfrich, H. Hutter, M. Schreiner, *Corros. Sci.* **2008**, *50*, 1112.

[30] J. P. Franey, G. W. Kammlott, T. E. Graedel, *Corros. Sci.* **1985**, *25*, 133.

[31] H. E. Bennett, R. L. Peck, D. K. Burge, J. M. Bennett, *J. Appl. Phys.* **1969**, *40*, 3351.

[32] R. Cortes, M. Froment, A. Hugot-Le Goff, S. Joiret, *Corros. Sci.* **1990**, *31*, 121.

[33] B. Zhang, J. Wu, X. Li, H. Liu, B. Yadian, R. V. Ramanujan, K. Zhou, R. Wu, S. Hao, Y. Huang, *J. Phys. Chem. C* **2014**, *118*, 9073.

[34] J. Park, H. Park, P. Ercius, A. F. Pegoraro, C. Xu, J. W. Kim, S.-H. Han, D. A. Weitz, *Nano Lett.* **2015**, *15*, 4737.

[35] H. Cho, M. R. Jones, S. C. Nguyen, M. R. Hauwiller, A. Zettl, A. P. Alivisatos, *Nano Lett.* **2016**, *17*, 414.

[36] S. Keskin, N. de Jonge, *Nano Lett.* **2018**, *18*, 7435.

[37] N. de Jonge, L. Houben, R. E. Dunin-Borkowski, F. M. Ross, *Nat. Rev. Mater.* **2019**, *4*, 61.

This article is protected by copyright. All rights reserved.

[38] G. Zhu, Y. Jiang, W. Huang, H. Zhang, F. Lin, C. Jin, *Chem. Commun.* **2013**, *49*, 10944.

[39] N. M. Schneider, M. M. Norton, B. J. Mendel, J. M. Grogan, F. M. Ross, H. H. Bau, *J. Phys. Chem. C* **2014**, *118*, 22373.

[40] D. L. Engelberg, in *Shreir's Corrosion*, (Eds: B. Cottis, M. Graham, R. Lindsay, S. Lyon, T. Richardson, D. Scantlebury, H. Stott), Elsevier, Oxford 2010, 810.

[41] L. Han, Q. Meng, D. Wang, Y. Zhu, J. Wang, X. Du, E. A. Stach, H. L. Xin, *Nat. Commun.* **2016**, *7*, 13335.

[42] S. Dai, Y. Hou, M. Onoue, S. Zhang, W. Gao, X. Yan, G. W. Graham, R. Wu, X. Pan, *Nano Lett.* **2017,** *17*, 4683.

[43] S. Dai, Y. You, S. Zhang, W. Cai, M. Xu, L. Xie, R. Wu, G. W. Graham, X. Pan, *Nat. Commun.* **2017**, *8*, 204.

[44] W. Xia, Y. Yang, Q. Meng, Z. Deng, M. Gong, J. Wang, D. Wang, Y. Zhu, L. Sun, F. Xu, J. Li, H. L. Xin, *ACS Nano* **2018,** *12*, 7866.

[45] S. F. Tan, S. W. Chee, Z. Baraissov, H. Jin, T. L. Tan, U. Mirsaidov, *Adv. Funct. Mater.* **2019**, *29*, 1903242.

[46] D. B. Butrymowicz, J. R. Manning, M. E. Read, *J. Phys. Chem. Ref. Data* **1973**, *2*, 643.

[47] A. B. Taylor, A. M. Siddiquee, J. W. M. Chon, *ACS Nano* **2014**.

[48] Z. Falkenstein, M. Hakovirta, M. Nastasi, *Thin Solid Films* **2001**, *381*, 84.

[49] Y.-S. Kang, H. Lee, Y.-M. Kang, P. S. Lee, J.-Y. Lee, *J. Appl. Phys.* **2001**, *90*, 5940.

[50] Y.-S. Kang, H. Lee, S.-C. Park, P. S. Lee, J.-Y. Lee, *J. Electrochem. Soc.* **2001**, *148*, A1254.

[51] E. Touzé, C. Cougnon, *Electrochim. Acta* **2018**, *262*, 206.

[52] s. B. Adeloju, Y. Y. Duan, *Br. Corros. J.* **1994**, *29*, 309.

[53] J. S. Du, P.-C. Chen, B. Meckes, Z. Xie, J. Zhu, Y. Liu, V. P. Dravid, C. A. Mirkin, *Angew. Chem. Int. Ed.* **2017**, *56*, 7625.

[54] J. S. Du, P.-C. Chen, B. Meckes, E. J. Kluender, Z. Xie, V. P. Dravid, C. A. Mirkin, *J. Am. Chem. Soc.* **2018**, *140*, 7213.

[55] K. Dabov, A. Foi, K. Egiazarian, in *15th European Signal Processing Conference*, 2007, 145.

Author Manuscript

This article is protected by copyright. All rights reserved.

16163028, 2021, 46, Downloaded from https://onlinelibrary.wiley.com/doi/10.1002/adfm.202105866 by Office Of Scientific And Technical Information, Wiley Online Library on [30/08/2023]. See the Terms and Conditions (https://onlinelibrary.wiley.com/terms-and-conditions) on Wiley Online Library for rules of use; OA articles are governed by the applicable Creative Commons License

16163028, 2021, 46, Downloaded from https://onlinelibrary.wiley.com/doi/10.1002/adfm.202105866 by Office Of Scientific And Technical Information, Wiley Online Library on [30/08/2023]. See the Terms and Conditions (https://onlinelibrary.wiley.com/terms-and-conditions) on Wiley Online Library for rules of use; OA articles are governed by the applicable Creative Commons License

Author Manuscript

Hetero-bimetallic nanoparticles undergo galvanic corrosion when exposed to aqueous environments and transform into unusual half-spheroids. In a Ag-Cu model system, Cu is sacrificially etched in a fractal manner prior to Ag due to a lack of protective surface oxide, as revealed by *in situ* electron microscopy. An Ar plasma generates crystalline CuO on Cu surface, which significantly enhances particle stability.

Jingshan S. Du, Kun He, Yaobin Xu, Carolin B. Wahl, David D. Xu, Vinayak P. Dravid*, Chad A. Mirkin*

Galvanic Transformation Dynamics in Heterostructured Nanoparticles

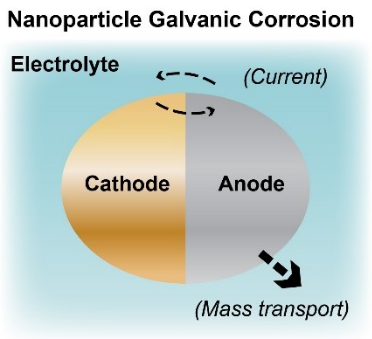

This article is protected by copyright. All rights reserved.